Development of 2D GEM-based SXR plasma imaging for DTT device: focus on readout structure

Maryna Chernyshova[a], Karol Malinowski[a], Sławomir Jabłoński[a], Irene Casiraghi[b], Iraida N. Demchenko[c] and Yevgen Melikhov[d,e]

[a]*Institute of Plasma Physics and Laser Microfusion, Hery 23, 01-497 Warsaw, Poland*
[b]*University of Milano-Bicocca, Piazza dell'Ateneo Nuovo, 1, 20126 Milan, Italy*
[c]*Laboratory of Electrochemistry, Department of Chemistry, University of Warsaw, Pasteura 1, 02-093 Warsaw, Poland*
[d]*School of Engineering, Cardiff University, CF24 3AA, Cardiff, U.K.*
[d]*Institute of Fundamental Technological Research, Polish Academy of Sciences, Pawinskiego 5B, 02-106 Warsaw, Poland*

Creation and development of a new diagnostics useful for future thermonuclear reactors and helpful in studying impurity profiles, MHD modes/localization, and imaging are among urgent tasks in plasma research field. Global SXR imaging for DTT device in support of power exhaust programme and its consecutive impact for plasma core is an example of applicability of such diagnostics.

This contribution presents the results of the ongoing development of the elaborated plasma X-ray imaging technology focusing on the design of the relevant structure of readout electrode. In order to achieve that, the details on the expected plasma radiation for the selected scenario for DTT machine were assessed. Then, the spatial distribution of plasma radiation intensity flux that will be reaching the detector window of the GEM based detector was simulated. Taking it into account along with the physical properties of the detector, the spatial and temporal distributions of charge cloud that will be reaching the readout plane were evaluated. The special design of the readout structure has been proposed that fulfil critical conditions originated from technological and physical constraints. The final effectiveness of the GEM based detector was evaluated proving that such detector is well suited for an effective plasma radiation imaging.

Keywords: X-ray detectors; GEM detector simulations; Gas-electron multiplier (GEM) detector; SXR plasma imaging; DTT device;

1. Introduction

The "Divertor Tokamak Test facility" (DTT) [1], a fully superconducting tokamak, is devoted to integrate the most relevant physics and technology issues essential in future fusion plants. Together with the incorporation of the best divertor concept another major goal is to study particle and power exhaust problem under two fundamental conditions being an integrated environment and DEMO relevant conditions.

Power exhaust problem is an immediate problem to tackle for the next generation devices. While the development of the plasma radiation monitoring technology is not directly linked to the problem of power and particle exhaust, it is helpful in studying the specific issues caused by the material erosion growing from the interaction with the plasma. Such a knowledge is quite crucial for W based materials since only small amounts of W could be tolerated in thermonuclear plasmas due to its high radiative efficiency [2]. Contamination of plasma by metallic impurities and further interplay between particle transport and MHD activity, may lead to impurities accumulation, and, eventually, to disruption of the thermonuclear fusion reaction. The ITER and DEMO oriented machines are designed with the optimized spatial distribution of the magnetic field aiming to minimize region of interaction between the confined plasma and the Plasma-Facing Components (PFCs). This will lead to a decrease of the power flux on the PFCs and enlarge the particle exhaust by reaching favorable plasma conditions at the divertor [3]. In addition, if the edge plasma density is increased and impurities are forced into the Scrape-Off Layer (SOL) region, heating power that reaches PFCs/divertor could be lowered down, via impurity irradiation, aiming to reach strategic values of 5-10MW/m^2, i.e., the values with which the current, or near-future materials can cope [4].

Considering the above-mentioned, the proposed here new plasma radiation monitoring technology for SXR measurements will be of a relatively high importance to ITER/DEMO test devices. With the ability to monitor and understand behavior of W or other impurities in plasma, this technology could assist in resolving some of the pivotal problems, such as: influence of impurity contamination of the core on fusion performance and the ways to neutralize that; ability for a bulk plasma to have very high radiation fraction; impact of erosion and temperature; etc. [4].

Additionally, processes that occur during the interaction of radiation with matter in fusion facilities demand that materials used in such facilities are having an excellent radiative stability. This requirement is imposed on the wall materials as well as on other materials that are constituents of detectors. For example, large neutron fluxes of the tokamak environment may lead to a rapid degradation of current X-ray detectors. Hence, development of new technologies in the field of plasma diagnostics is quite timely, with the ultimate

intention for this technology to be used in future thermonuclear reactors.

This work addresses such a particular task. The proposed development is devoted for performing the global Soft X-Ray (SXR) *straight* 2D imaging which can provide valuable information on particle transport and magnetic configuration exceeding abilities of existing 1D tomography systems in the SXR region. The crucial element of such an imaging system is modern Gas Electron Multiplier (GEM) [5] detector adapted to register soft X-ray radiation (~2-15 keV) coming from a tokamak plasma. Ability to discriminate energy (about 17-25%) of the incident absorbed photons is one of the strengths of such detecting system, together with the ability to localize their positions on the detector readout pads (spatial resolution of up to a few hundreds of μm can be achieved). Among other advantages one can also acknowledge good temporal resolution (about 1 ms), compactness (variety of size and shape is available) and better neutron resilience (withstanding higher doses than solid state detectors).

The GEM based detector, being the core element of the developed system, has an important imbedded feature in its design: the processes of charge transfer/amplification are spatially separated from charge collection (i.e. signal reading) zone. Relative complexity of GEM based detector instigates an ongoing research in optimization of its response. Recent studies on influence of geometry of foils and holes [6], [7], on optimization of electric field distribution [8], and on influence of composition and flow rates of working gas mixture [9], have been aimed to improve the response of the GEM based detector affecting processes of charge transfer/amplification. Similarly, the response of the GEM based detector can be improved in charge collection zone since accumulated signal from the electron cloud should be extracted effectively and then correctly transferred into further electronics. The micro patterned readout plane geometry also significantly influences spatially resolved capabilities of the GEM based detector.

Within the scope of this task the most crucial for 2D imaging element of the detecting chamber was planned to be designed to focus on W and seeded impurities emission and cover photon range suitable for monitoring in the SXR region. For this purpose, the 2D readout board was designed and studied in an effort to verify its applicability as a divertor view DTT diagnostics. Both the expected ultimate intense photon rates and maximal achievable spatial resolution were accounted to define its suitability for effective plasma radiation imaging by the GEM based detector. This would allow effective monitoring of the core plasma, X point radiation and studying diverse phenomena such as, for example, tungsten transport and its interplay with MHD in tokamak plasmas. Coupled with the advanced fast high-performance electronics, such a system could monitor plasma radiation offering excellent space and good time resolution, as well as a charge spectrum from which the photon spectrum can be deconvoluted.

The paper is structured as follows. Section 2 addresses data and methods that were used for the simulations of the expected spectra and describes the procedure to simulate spatial and spectral distributions of the plasma radiation intensity flux that will be reaching the detector window. Knowing this and taking into account the physical properties of the GEM based detector, the spatial and temporal distributions of charge cloud that will be reaching the readout plane are evaluated and this procedure is described in Section 3. To ensure effective collection of the coming charge cloud, the special design of the readout structure has been proposed and is explained in Section 4, together with evaluation of final effectiveness of the GEM based detector. Finally, Section 5 summarizes the paper with the conclusions.

2. Data and methods exploited for simulations of plasma radiation spectra

In order to develop the desired readout structure, simulations of the expected SXR spectra were performed using the coronal equilibrium assumption. This allowed an overall assessment of the photons observed by each of the diagnostics' lines of sight (LOS). For tomographic reconstructions of the plasma parameters, for which the detailed knowledge about impurities distribution is important, more advanced calculations could have been employed with transport effects taken into account. For example, in the case of tungsten transport modelling advanced GKW (Gyro-Kinetic Workshop) software tool and neoclassical calculations are very often used, since this effect has to be considered. Nevertheless, even simplified but fast calculations, based on the coronal balance model, can provide answers to questions related to the load of SXR diagnostics pixels and, thus, contribute towards the design and commissioning phases of the new types of detectors built for specific plasma devices.

The detector was assumed to be a 2D pixel Triple-GEM detector [10], [11] with 5/2/2/2 electrode distances. The detector's position, shown schematically in Figure 1, was chosen with the following two objectives in mind: (i) coverage of the whole plasma view at the equatorial plane is required, and (ii) intrinsic detector saturation limits, $\sim 10^5 cps/mm^2$ of the absorbed photons should be aimed at (in order to elaborate the readout structure capable to sustain the maximal photon flux). In case the absorbed flux is above this limit, the detector's amplification starts to vary strongly with the incident intensity due to the space charge accumulation. In order to attenuate the intensive plasma emission, the diameter of a pinhole within the set-up was assumed to be of 20 μm. The pinhole was distanced by about 3 m and 0.2 m from the equatorial plane and the detector window, respectively. The diameter of the pinhole used for calculations, assuming a plate thickness is greater than zero and in combination with other dimensions determining the geometry of the GEM detector, may lead to a conclusion that the pixels located farthest from the center will not be able to register the plasma radiation due to the cylindrical shape

of the pinhole. However, by changing the cylindrical shape of the pinhole to a conical one, this problem can be overcome. Additionally, the thickness of the pinhole plate can be reduced with the use of appropriate materials with high Z. No further considerations (regarding, e.g., magnetic field impact, etc.) were taken into account.

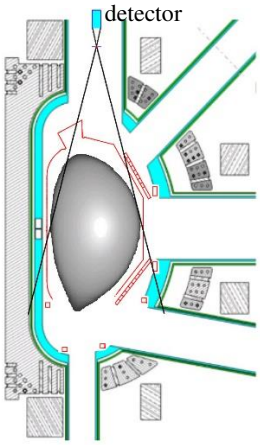

Figure 1. Scheme of the considered preliminary experimental setup of the detector positioning (not to scale).

It should be noticed that size of the readout pattern elements needs to be matched with the scale of the electron avalanche spot at the anode plane. Taking into account its dependence on the photon energy (see Fig. 2 in [10]), the detector readout structure was chosen in the form of hexagon pixels of 0.35 mm side pitch. The choice of pixel's size and shape was made aiming to achieve the best possible spatial resolution of the photon position determination as well as to collect the reasonable signal from a single pixel. This means that, in the case of the interconnection of several pixels in one independent electronics channel, unambiguous determination of the electron cloud (originating from a single photon absorption) on the readout plane could be achieved (see, for example, [12], [13], [10]). The standard detector size of 100x100 mm^2 is then covered by 34816 of identical pixels.

In order to support the DTT project and especially to provide scenarios for the diagnostic design, first-principle based multi-channel integrated modelling of main operational scenarios is needed. In such simulations, the transport equations for particle, momentum, and heat are solved using a first-principle transport model taking into account the non-linear interactions between the different transport channels and between the plasma and the heating systems, in a self-consistent magnetic equilibrium.

Particularly, this work is based on plasma profiles resulting from the simulation of the Single Null (SN) H-mode Full Power (FP) scenario with the option A heating mix. In the FP option A configuration, auxiliary heating systems provide a total power of ~46.8 MW to the plasma: ~15.0 MW from the NNBI (negative neutral beam injection) system (2 beams at 400 keV), ~3.0 MW from the ICRH system (60-90 MHz antennas), and ~28.8 MW from the ECRH system (170 GHz gyrotrons). The integrated modelling of the DTT steady-state Deuterium plasma of the FP option A scenario was carried out with the ASTRA [14] transport solver, using the Trapped-Gyro-Landau-Fluid (TGLF) SAT1 quasi-linear transport model [15], [16], [17]. The heating depositions were calculated by the JINTRAC [18] suite, with an iterative ASTRA-JINTRAC approach.

The temperature and density radial profiles are predicted within the top of the pedestal, whose values are used as boundary condition; the pedestal profiles were formerly calculated by the Europed code [19] with the EPED1 model [20]. Argon and Tungsten are included as impurities. The toroidal rotation is predicted using theory-driven formulas for the Prandtl and pinch numbers. All details on these integrated scenario simulations are reported in [21].

The radial profiles of electron temperature and density are shown in Fig. 2 as a function of the normalized effective minor radius $\rho_{tor} = \sqrt{(\Phi/\pi B_{tor})/(\Phi/\pi B_{tor})_{max}}$, where Φ is the toroidal magnetic flux and B_{tor} is the toroidal magnetic field. The central electron temperature is quite large (~15 keV) because of the large ECRH power density. The electron density has a moderately peaked profile, reaching a maximum value of ~$2.5 \cdot 10^{20} m^3$.

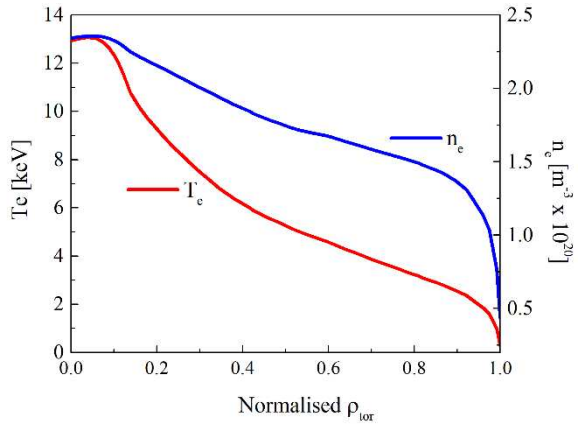

Fig. 2. Electron temperature T_e and electron density n_e radial profiles of the DTT full power SN scenario.

The considered Ar (0.1932 %) and W (0.00942 %) impurity levels were used together with the calculated 2D maps of T_e, n_e to simulate the foreseen spectra at the GEM detector. The electron temperature, electron density and impurity profiles along the detector's LOS were exploited to obtain the integrated emissivity of SXR spectrum along a given LOS. The calculations under coronal equilibrium [22] took into account the adopted geometry of the detector, its size and location relative to the plasma as well as the size, shape and position of the pinhole. As a result, an X-ray spectrum for each pixel of the GEM detector was produced, where

the main mechanisms of soft X-ray emission are considered. Those are free-free emission (bremsstrahlung), free-bound emission (recombination radiation) and bound-bound emission (line radiation).

Bremsstrahlung, an electromagnetic radiation produced by a deceleration of a charged particle in the electric field of another charged particles, typically free electron in atomic nucleus field, expressed by emission energy per unit frequency $d\omega$, temporal interval dt and unit volume dV, averaged over the Maxwell velocity distribution and summed over all species of ions j, is given by [23], [24], [25], [26], [27]:

$$\frac{dE_{ff}}{d\omega dtdV} = \sum_j \frac{16}{3}\left(\frac{2\pi}{3}\right)^{\frac{1}{2}}\left(\frac{e^2}{4\pi\varepsilon_0 c}\right)^3 \frac{n_e n_j Z_j^2}{m_e^{\frac{3}{2}}(k_B T_e)^{\frac{1}{2}}}\bar{G}_{ff} e^{-\frac{\hbar\omega}{k_B T_e}}, \quad (1)$$

where m_e and T_e are the electron mass and temperature, $\hbar\omega$ - the emitted photon energy, n_j - the ion density for the charge Z_j, and $\bar{G}_{ff}$ is the temperature-averaged free-free Gaunt factor calculated in the assumption of Boltzmann distribution.

When free electrons are captured by plasma ions, the second kind of electromagnetic radiation could be observed [23], [24], [25], [26], [27]:

$$\frac{dE_{fb}}{d\omega dtdV} = \sum_j \frac{16}{3}\left(\frac{2\pi}{3}\right)^{\frac{1}{2}}\left(\frac{e^2}{4\pi\varepsilon_0 c}\right)^3 \frac{n_e n_j Z_j^2}{m_e^{\frac{3}{2}}(k_B T_e)^{\frac{1}{2}}} e^{-\frac{\hbar\omega}{k_B T_e}} \cdot \left[\frac{\chi_{j-1}}{k_B T_e}\bar{G}_{fb}(n)\frac{\xi}{n^3} e^{-\frac{\chi_{j-1}}{k_B T_e}} + \sum_{\mu=n+1}^{\infty}\bar{G}_{fb}(\mu)\frac{Z_j^2\chi_H}{\mu^2 k_B T_e}\frac{2}{\mu} e^{-\frac{Z_j^2\chi_H}{k_B T_e}}\right], \quad (2)$$

where χ_{j-1} is the ionization potential of the final ion with charge *j-1*, n - the main quantum number of this state, $\xi = 2n^2$ is the total number of places in the shell with the main quantum number n , and $\bar{G}_{fb}(n)$ - the Gaunt factor for the recombination to the n-th shell. Whereas Bremsstrahlung produces a continuous spectrum, free-bound radiative recombination emission additionally generates discrete edges.

The third main component of the SXR spectrum is line radiation, which is emitted due to an electron transition from a higher to a lower energy state within ion/atom. The emitted photon energy is equal to the difference between initial and final quantum states. There exist many possible electron transitions per a given ion/atom, which have specific discrete energies. Such a group of different transitions, resulting in specific radiated wavelengths, composes a line emission spectrum with emission energy per interval dt and unit volume dV [27], [28], [29]:

$$\frac{dE_{bb}}{dtdV} = Kn_e n_i \sum_j \frac{f_j \bar{G}_{bb}\sqrt{E/k_B T_e}}{E^{\frac{3}{2}}} e^{-\frac{E}{k_B T_e}} E_j,$$

$$\bar{G}_{bb} = A + (B\cdot y - C\cdot y^2 + D)e^y \cdot E_1(y) + C\cdot y\ , \quad (3)$$

where K is normalization factor, n_e and n_i - electron and ion densities, f_j - an oscillator strength, $\bar{G}_{bb}$ - an averaged Gaunt factor of Mewe interpolation for bound-bound emission, E and T_e - excitation energy and electron temperature, E_j - energy of the X-ray photon, A, B, C, D - Mewe parameters in SI units, E_1 - exponential integral function, $y = E/k_B T_e$.

All the introduced equations represent emission from a localized plasma unit volume, dV. Thus, the total calculated spectrum for each detector pixel is a sum of plasma radiating points inside its cone of view.

The equations (1)-(3) depend on the electron temperature and density, as well as on the ion density. The calculations use 2D input data of T_e and n_e, which are usually derived from the experimentally obtained and manually adjusted 1D profiles but in this case they were simulated as described above. The ion densities are calculated assuming coronal equilibrium using T_e and n_e profiles by solving the kinetic equations:

$$\frac{\partial n_i}{\partial t} = 0 = S_{i-1}n_e n_{i-1} - S_i n_e n_i + \left(R_{i+1} + R_{i+1}^{CX}\cdot\frac{n_0}{n_e}\right)\cdot n_e n_{Z+1} - \left(R_i + R_i^{CX}\cdot\frac{n_0}{n_e}\right)n_e n_Z, \quad (4)$$

where S_i is the rate coefficient for electron impact ionization, R_i , R_i^{CX} - radiative and charge-exchange recombination coefficients, n_i - ion density of charge state i, n_e and n_0 - electron and neutral densities.

In addition to the basic equations describing the X-ray emission from plasma, one should also take into account the additional contribution related to the linear emission by the de-excitation processes associated with the charge-exchange recombination process. However, as can be seen from the equation (5), the amount of this radiation depends strongly on both the ion density of plasma impurities and the density of non-ionized hydrogen $n_{H(0)}$. In the considered case, due to the high electron temperatures within the dominant part of the plasma radius, the $n_{H(0)}$ density is low, what limits the charge-exchange contribution to the total radiation:

$$\frac{dE_{XC}}{dtdV} = P_{XC} \approx 1.6\cdot 10^{-13} n_{H(0)} n_z \langle\sigma v\rangle_{CX}\chi_{Z-1}, \quad (5)$$

where $n_{H(0)}$ neutral hydrogen density, n_z -density of the ion with charge Z, χ_{Z-1} - ionization potential of the ion with charge *Z-1*.

The results of calculations presented here were made for Hydrogen plasma with the essential parameters, e.g., effective ionization and recombination coefficients, being readily available from existing databases. It is estimated that selection of Deuterium instead of Hydrogen will have a negligible effect on the

results. Choosing the appropriate essential parameters and assuming the local charge balance, the calculations were performed to evaluate fractional abundances and densities for all the impurity ions. The considered photon energy was in the range from 80 eV up to 15 keV. The atomic spectroscopic data were based on Open ADAS database. All data are gathered in ADF15 sub database.

The 2D map of the radiation intensity flux over the whole detector window per each individual pixel is shown in Figure 3 for the divertor view detector.

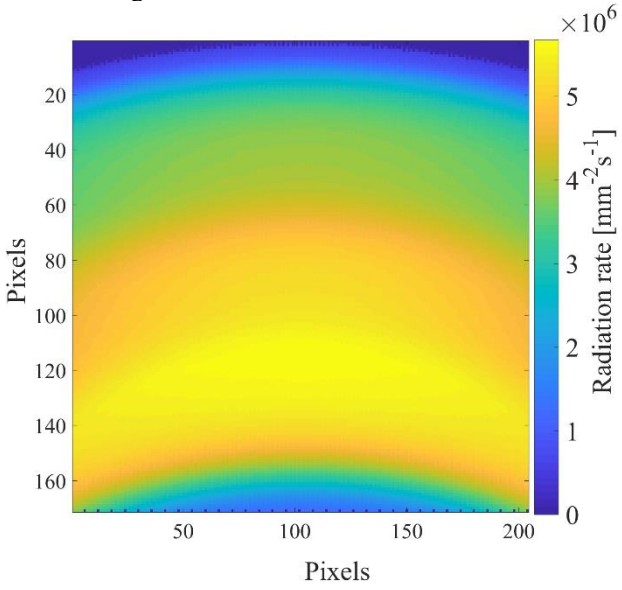

Figure 3. The calculated 2D intensity map for the divertor top view detector.

Figure 4 shows the obtained spectra in the range of 0.08-15 keV for a few pixels with the diverse intensity of the incoming radiation. The spectra are quite similar for all the readout pixels, differing mainly in the intensity values, except for the edge plasma, where W emission at about 2 keV gradually vanishes.

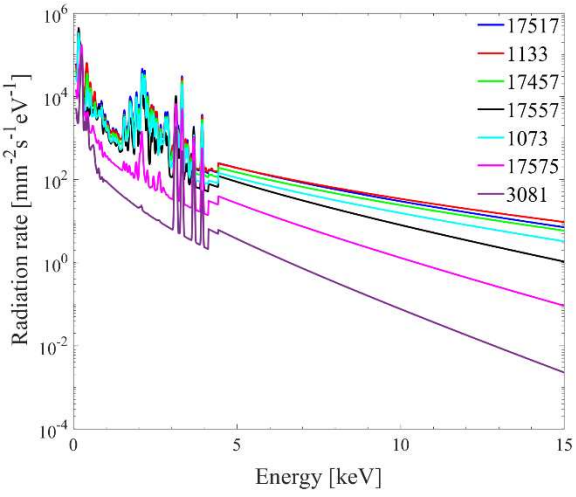

Figure 4. The calculated SXR spectra expected from the plasma within the integrated LOS assigned to the detector pixels. A few pixels (LOS) are selected with the different intensity load, including pixels that are subject to the most and the least photon fluxes.

3. Simulations of the detector's signal distribution under the expected SXR radiation

In the next step, the data obtained in Section 2 (Figures 3-4) were used to compute the full picture in time and space of the detector signals on the readout electrode taking into account the detector's efficiency and its internal work principles

The processing procedure was as follows. Initially, all the original spectra for every pixel were attenuated by Be 50 μm filter [30], which is usually used as a pinhole material, cutting off all the quanta below ~1 keV. The filter's material was required to fulfil the following two requirements: a decrease of the total flux intensity, and retention of as much radiation as possible in the region 2-3 keV corresponding to W emission. Additionally, the spectra were processed according to the GEM detector's efficiency, calculated by GEANT4 code [31] considering gas working medium and taking into account the entire detector's structure of the triple-GEM filled with Ar/CO_2 of 70/30 ratio. The Detective Quantum Efficiency (DQE), after taking 50 μm Be filter transmission into account, is shown in Figure 5. Two absorption edges are observed in the dependence: the first peak at about 3.2 keV, resulting from the binding energy of electrons in the K-shell of Ar, which is the basic component of the gas mixture, and the second one at the energy of about 9.0 keV, related to the K-edge of Cu, which is the main material of the GEM foils (thin perforated Kapton foils both sides covered with thin Cu layer). The impact of the DQE onto the original spectrum is presented in Figure 6. It should be mentioned that depending on the research target the attenuating filter could be tuned, up to a certain extent, in order to focus on another impurity emission, for example, Ar line radiation, in the SXR region. The implied modification of the spectrum is seen in the Figure 6 together with the original one (above 1 keV).

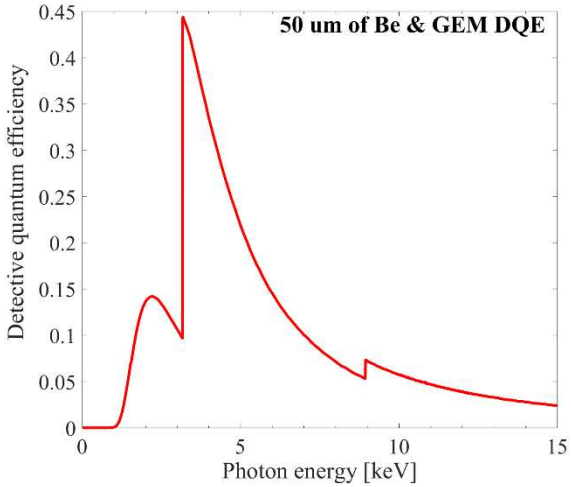

Figure 5. GEM detector quantum efficiency taking into account Ar/CO_2 gas mixture of 70/30 ratio and internal structure of the detecting chamber, augmented by the Be filter transmission.

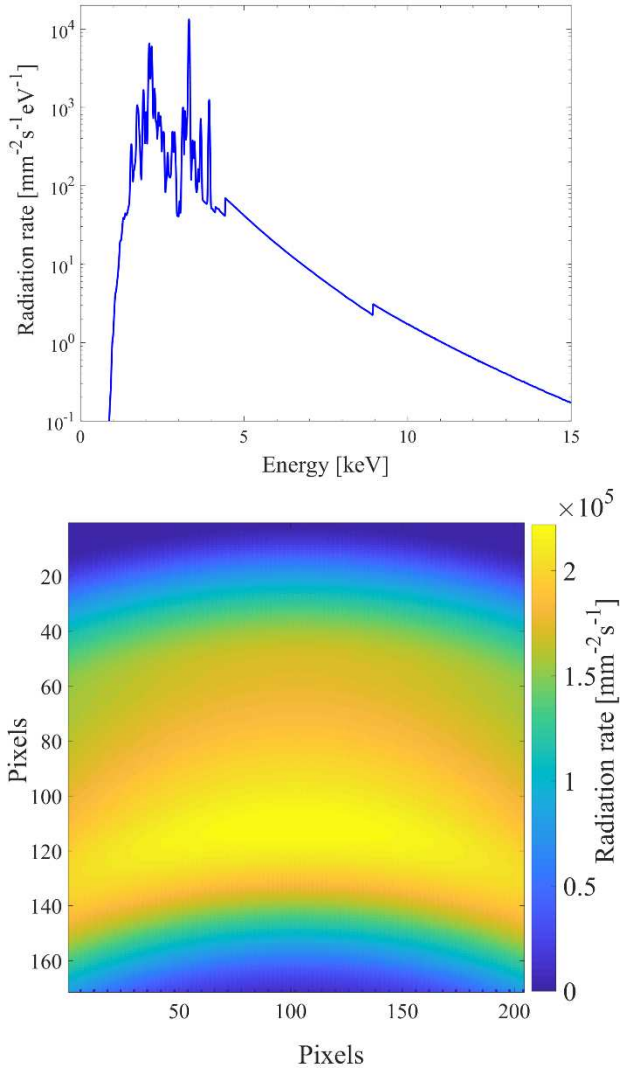

Figure 6. The expected plasma radiation filtered by 50 μm of Be and processed with application of GEM DQE. Top: spectrum for #17517, one of the pixels subjected to the most intensive radiation. Bottom: 2D intensity map of the absorbed photons with the mean and maximal rate of 1.42 and $2.22 \cdot 10^5 cps \cdot mm^{-2}$, respectively.

In the next step, taking into account photon intensity per second from Figure 6 for each pixel, a random distribution of X-ray incidence time points onto the pixel surface was generated within a chosen time interval of 1 ms (this corresponds to the LOS for a given pixel). In this way, time evolution/stamping of the incoming absorbed photons was obtained for each pixel composing the total picture of the temporal distribution of the recorded radiation at the detector.

Then, a given energy of the incident photon is drawn according to the spectrum for the chosen pixel (see, e.g., Figure 6). For the selected photon energy, an average number of primary electrons, created in the detector conversion gap, is estimated. This number is assumed to have the distribution for 5.9 keV photon energy as in [32] and is assumed to be proportional to the δ-electron energy (energy of photoelectron from the initial photon absorption). Probability of the exact number of primary electrons for a given value of the average number of primary electrons (at a given energy of the δ-electron) is described by the Gaussian distribution: $P = \mathrm{A} \cdot \exp(-(N_e - \overline{N_e})^2/(2\sigma^2))$, where A is the normalized amplitude, i.e. $\mathrm{A} = 1$, N_e – number of primary electrons, $\overline{N_e}$ – mean number of primary electrons for a given photon energy. Its FWHM varies proportionally to the square root of the average number of primary electrons, $\sigma = \sqrt{\overline{N_e}}/2.3548$ [33].

Generally, for a given energy of the δ-electron, the corresponding primary electron number is obtained using Box-Muller transform to generate random values with normal (Gaussian) distribution as follows: $B = \sqrt{-2 \cdot \log(u_1)} \cdot \cos(2\pi \cdot u_2)$; $N_e = B \cdot \sigma + \overline{N_e}$, where u_1, u_2 are the random numbers. In this way, for the given average number of primary electrons, a specific value of primary electrons number is drawn at random from the Gaussian distribution with known parameters.

In the following steps, it is assumed that amplitude of primary electron distributions (both temporal and spatial) on the readout is proportional to the obtained number of primary electrons. Two examples of temporal distribution for two HV configurations of 1500/700/700/900 V and 600/400/500/800 V (for all the gaps starting from the detector window up to the induction gap) are shown in Figure 7 (a) and (b), respectively, for 5.9 keV photons. The time shown refers to the duration (~155 ns and ~210 ns) of the avalanche movement from its initiation (photon absorption) in the drift region to the moment it reaches the readout plane. Detector amplification was selected to have rather lower gain but with faster electron avalanche since the calculated intensity load of each pixel is extremely high. The selected time duration of the electron avalanche was applied for all the photons from the original spectrum. For the further considerations, the faster signal was taken into account. This dependence was fitted by an analytical function (shown in Figures 7 (a-b)) used afterwards for the whole set of the primary electron numbers. For the simplicity of calculations, signal duration was kept as the one for distribution in Figure 7 (a) whereas distribution amplitude was varied with the primary electron number.

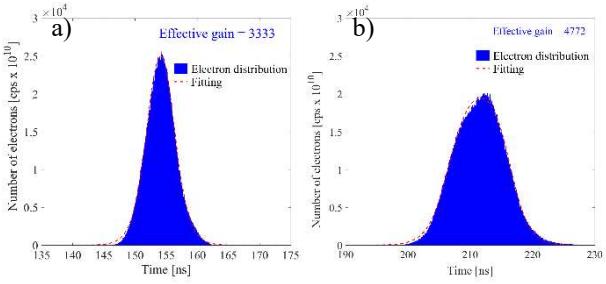

Figure 7. Simulated time distributions of the GEM-detector signal arriving at the readout plane (independently on the pixel/anode structure) for two HV configurations: (a) 1500/700/700/900 V, faster with lower gain and (b) 600/400/500/800 V, slower with higher gain for the same HV applied to the GEM foils, 380 V. Time bin was taken as 0.1 ns.

For each pixel, the (X, Y) position of the incoming photon is chosen at random, assuming equal probability of photon appearance position over the whole surface of the pixel. Distribution of the electrons due to spreading onto neighboring pixels is also considered. Time distributions with amplitudes proportional to the number of electrons are assigned to the quantities of electrons distributed over a few pixels. Finally, the result of temporal distribution for each pixel is saved in the form of its starting time and amplitude (with fixed duration). This procedure of determining the photon time distribution on the readout is repeated for 1 ms interval, considering the signals from the enabled neighboring pixels which constitute a cluster from a single photon. It is assumed also that temporal distribution of readout electrons is the same for any of XY coordinates.

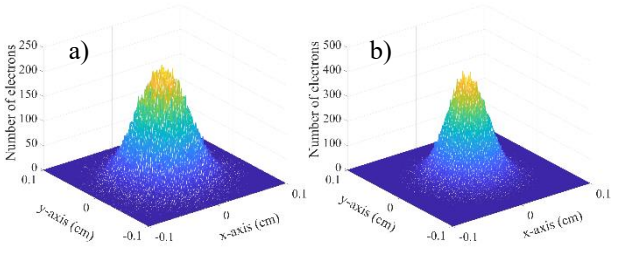

Figure 8. The simulated 3D spatial distributions of the electron avalanche from a single 5.9 keV photon on the readout plane for two HV configurations of (a) 1500/700/700/900 V and (b) 600/400/500/800 V for the same HV applied to the GEM foils, 380 V.

Spatial distribution of the electron avalanche on the readout plane was simulated by Garfield++ for given HV configurations and 5.9 keV photons [34] (see Figure 8). It can be seen that the spatial distribution for higher HV configuration is wider (FWHM=0.67 mm) than for the lower one (FWHM=0.55 mm). This could be explained by the fact that for this range of electric fields the electron transverse diffusion increases with increasing electric field. There is also some contribution due to higher induction field (the last gap above the readout anode).

Spatial spread of the selected electron avalanche (Figure 8 (a)) onto the readout plane was fitted by Gaussian 2D fit, which was used for both coordinates, and was applied to the whole set of considered photons. This Gaussian 2D shape was used everywhere regardless of XY coordinates on the readout plane, whereas amplitude of this distribution varies with the δ-electrons energy, proportionally to the number of primary electrons. The electron distribution on the readout (2D Gaussian) is a spatial histogram of high density, so it can be divided into pixels as accurately as needed. The sums of electrons from the distribution are assigned to specific pixels, which cover the total spatial distribution around the XY center. The cut-off for the electron number at each pixel is assumed to be at the level of 3% of the total electrons number produced by 5.9 keV photon. The assumed cut-off does not influence the total number of the detected photons, nevertheless it worsens the photon energy estimation, mainly of the low energy photons. The assumed threshold would affect the 2-3 keV photons by 17-12% losses/cut-off of their energy. For 5 keV photons the losses are at the level of 6%. The assumed value of the charge cut-off is hold within the intrinsic detector resolution as well as somewhat matches the currently used electronics sensitivity. Nevertheless, the smaller this threshold, the more precise photon energy estimation is. Therefore, within the future upgrade of the proposed structure this parameter will be optimized to keep it at least at the level of 1% cut-off related to 5.9 keV photon energy, which should improve the estimation of the photon energy losses down to 6-4% for 2-3 keV photons.

Examples of the electron avalanche projections onto the readout plane are shown in Figure 9 for two photon energy values of 1.2 keV (a-b) and 10 keV (c-d). Formation of the charge cluster, coming from a single photon, could be recognized within the assumed cut-off. Such a cluster identification was carried out for all the considered photons.

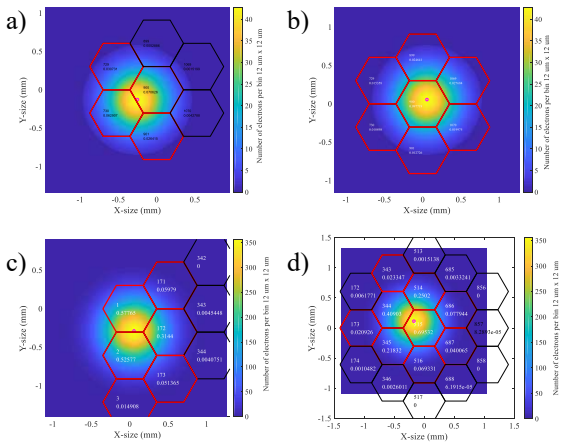

Figure 9. Electron avalanche spread onto readout plane with identification of pixels forming a charge cluster corresponding to a single photon absorption: (a-b) for 1.2 keV photon for pixel #900; and (c-d) for 10 keV for pixels #1 and #515.

Following all the steps described above the successive time evolution of the expected signals for the whole pixel map was found. To estimate the overlapping percentage of the signals it was assumed that two photons are considered separated if time interval between their maxima is such that a local minimum (understood as a sum of two time distributions) is 10% lower than the maximum of the smaller signal. This case is illustrated in Figure 10. The assumed value assures further separation of the pulses within the developed acquisition electronics [35] based on the elaborated algorithm [36] for the signal processing.

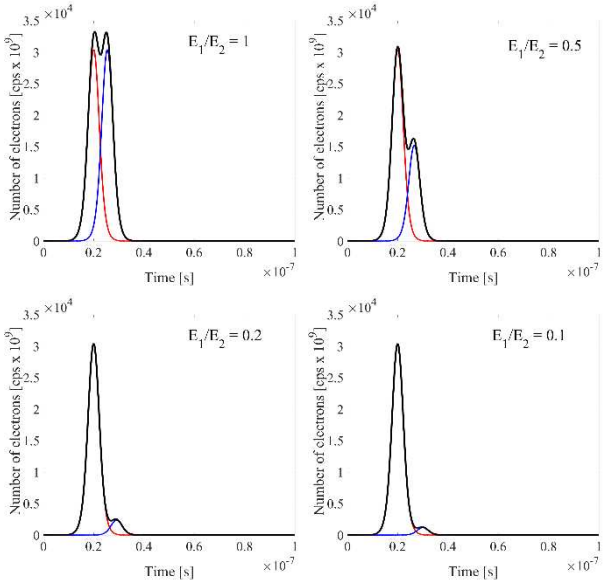

Figure 10. Illustration of signal overlapping for calculated temporal distributions assumed for 15 keV photons and photons with energy of different ratios (1:1, 2:1, 5:1, 10:1) to the considered photon energy (only amplitude is proportional to the photon energy).

Considering all the steps described above, the spatial and time distributions for each absorbed photon are obtained. An example of the temporal distribution of the detector signals coming from the detected photons on the individual pixel is shown in Figure 11. As can be concluded from the both Figures 11 (a) and (b), practically all the signals are distinguishable. There are mostly separated pulses at the readout plane with some overlapped ones, at the level of 2.74% for this pixel, not able to be separated using the developed algorithms [36].

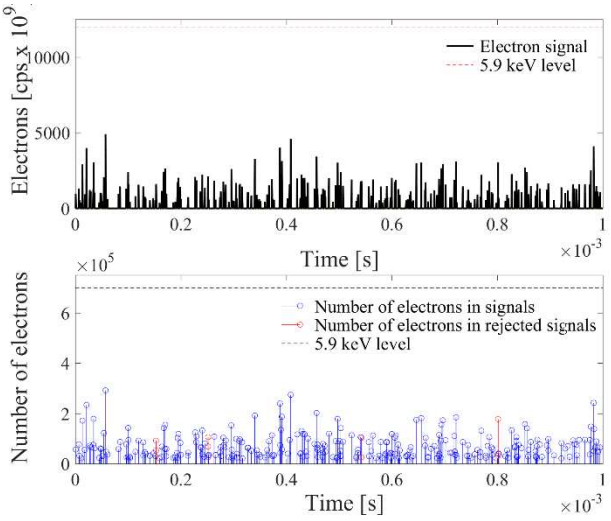

Figure 11. Example of the expected rate at the detector readout for one of the most intensive central pixels. Top: corresponding time signals at the readout anode for pixel #18529 at the rate of $9.17 \cdot 10^5 cps \cdot mm^{-2}$ ($2.92 \cdot 10^5 cps$ per pixel). Bottom: time stamps corresponding to electron signals with their integrated electron amount shown for 1 ms duration.

Taking into account all the above for the whole readout structure of individual hexagonal pixels, the total 2D map of the expected signal rate at the detector anode pattern was finally obtained. Avalanche spreading, the generated charge corresponding to the absorbed photon, onto a few neighboring pixels was taken into account. The signal rate map is shown in Figure 12 (a). As the hexagon pixels are of a smaller size than the avalanche spot on the readout plane, the signal rate exceeds significantly, by about 10 times, the expected photon rate (see Figure 6, bottom graph). The number of the overlapped signals in time per each pixel was found to be at the level of 1.3% (the average value, see Figure 12 (b)) for the central most intensive part of the detecting surface (within rows from 40 till 140) and is very low for this type of measurements. The higher values of the rejected fraction close to the plasma edge is related with the low photon intensity and therefore higher statistics for the overlapped signals.

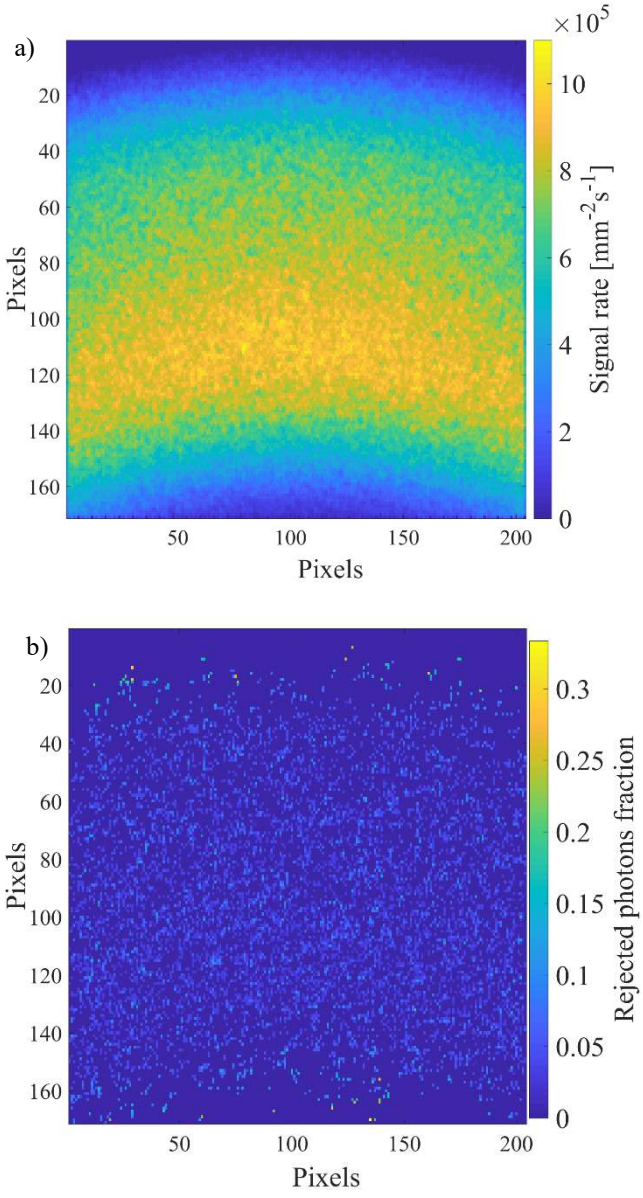

Figure 12. 2D maps of (a) the obtained signal rate at the individual pixel readout taking into account avalanche spreading onto a few neighboring pixels and (b) of the overlapped signals on the individual pixels readout.

4. The proposed readout structure and obtained results

As it was mentioned in Introduction, the goal of the present study was to achieve such a readout structure that is capable to fulfil both conditions: to collect (i.e. to determine energy and position) as many absorbed photons as possible up to the detector limits of 10^5 photons/mm^{2}s and to have reasonable number of the independent channels of electronics. Altogether, if one independent channel is assigned to an individual pixel, the detector with 34,816 pixels would require 34,816 channels, which is far greater than current electronics can cope with. In order to reduce the number of channels, interconnection between pixels is used in a way to account for signals pile-up and to maximize the board effectiveness. Here, considering symmetry of the detector avalanche and the calculated spatial distribution of the plasma radiation the following scheme of interconnecting pixels was proposed.

Eight basic independent groups of pixels, multipixels, were chosen to cover the hexagonal pattern of the readout board to compose the independent electronics channels. This pattern is presented in Figure 13. In order to explain this arrangement in details, let us first concentrate on 408 multipixels that belong to the groups XT and XB (where XT/XB stands for top/bottom division of the whole area of the readout for the variable X). Looking at the first column, pixel number 1 (global numbering) corresponds to XT1 multipixel, pixel 3 – to XT2, and this pattern XT1/Y…/XT2/Y… repeats until the end of the top half of this column. After that, the pattern XB2/Y…/XB1/Y… repeats until the end of the bottom half of this column (see Figure 13). The next XT/XB multipixels are assigned for the next column that is shifted horizontally by the half pitch with respect to this one (e.g., new independent multipixels XT3, XT4, XB3 and XB4 are introduced for the third column, and so on). This pattern is repeated every other column. Altogether, the total number of multipixels for XT/XB is 408. As seen in Figure 13, similar arrangements are organized for groups YL and YR (where YL/YR stands for left/right division of the whole area of the readout for the variable Y).

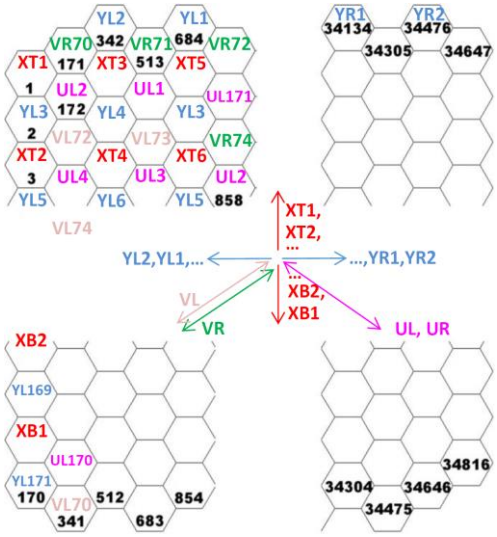

Figure 13. 2D map of the pixel readout showing all 34816 pixels that are interconnected into 1434 independent multipixels. Each multipixel corresponds to a particular independent electronics path/channel. All multipixels are split into eight independent groups labelled: X (top/bottom), Y (left/right), U (left/right) and V (left/right). Numbers in black color represent the pixel number. Numbers in other colors identify pixels that belong to the same multipixel in the respected group.

In case of multipixels that belong to UL/UR group, the left/right division of the whole area of the readout is a bit more complex (see Figure 14 for variable U). Each multipixel now is formed out of pixels that lie on the same hexagonal variable U (e.g., see pixels #172 and #858 that belong to the same multipixel UL2 in Figure 13). In this case, however, in order to keep similar number of pixels in every multipixel, one needs to create both uninterrupted and interrupted multipixels as shown in Figure 14. In the case of UL group, for example, there are 74 uninterrupted multipixels (all from UL1 till UL73 and UL171) with the total number of multipixels being 171. Multipixels for the groups VL/VR are constructed in the similar manner as for the groups UL/UR taking into account different direction of the hexagonal variable V. In general, it comes mostly to 21/22 and 25/26 pixels that are interconnected to form any multipixel, i.e. a single acquisition path.

In total, the readout board with the pixels arranged in this X, Y, U and V multipixels way holds 1434 independent channels of electronics. This number of independent channels is reasonably/safely lower than the limits of the recently developed processing modules [37]. And at the same time, such a number should still enable effective performance of high-speed electronics and data acquisition system.

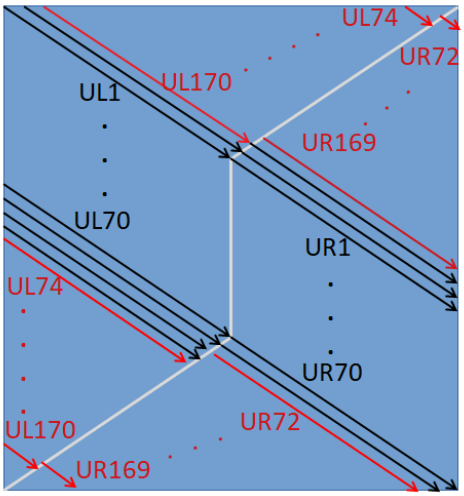

Figure 14. Arrangements of 342 multipixels for the group U (left/right). The white line shows the division of the whole area of the readout into left/right. Uninterrupted multipixels are represented by black lines; interrupted multipixels are represented by red lines. The total number of pixels in a particular multipixel is within 24-26 range depending on its position. Altogether, there are 171 multipixels in UL/UR groups.

As was mentioned for the considered readout structure with the over 30,000 of independent pixels, avalanche spreading throughout the detector expands the spatial distribution of the detector signals and enlarges the signal rate on the individual pixel. That is beneficial from the point of view of more precise photon position reconstruction. Simultaneously, the more pixels (smaller ones) participate in the processing of a single photon, the more independent channels are needed to collect the signals. Under this work, the pixel size choice was aimed at matching the avalanche spot and to involve at least 3-4 pixels into its identification. The interconnection of the pixels was elaborated so that all the pixels within a single charge cluster belong to different multipixel groups in order to avoid a complete overlapping of their signals. Such an overlapping makes it impossible to identify the photon energy and position unambiguously. That leads to a loss of this information, and therefore, such overlapped signals will be rejected for further analysis. In such a case, the processing algorithms will recognize overlapped signal estimating their amount to some extent. This parameter defines the effectiveness of the developed readout structure.

In order to estimate the effectiveness of the proposed readout pattern and to determine the amount of lost information, the foreseen rate on each multipixel was calculated. It was found that the level of $1.7 \cdot 10^6$ cps per multipixel surface for Y, U and V multipixel groups was reached, with a little bit less rate of up to $1.2 \cdot 10^6$ cps per multipixel for X groups. Amount of the rejected overlapped signals was also determined. It is presented in Figure 15 for all the multipixels together with the calculated fraction of the detected photons which were rejected from the analysis due to overlapping in time of at least one signal among the signals forming a cluster from a single photon. For this reason, the fraction of rejected photons is significantly higher than the fraction of rejected signals.

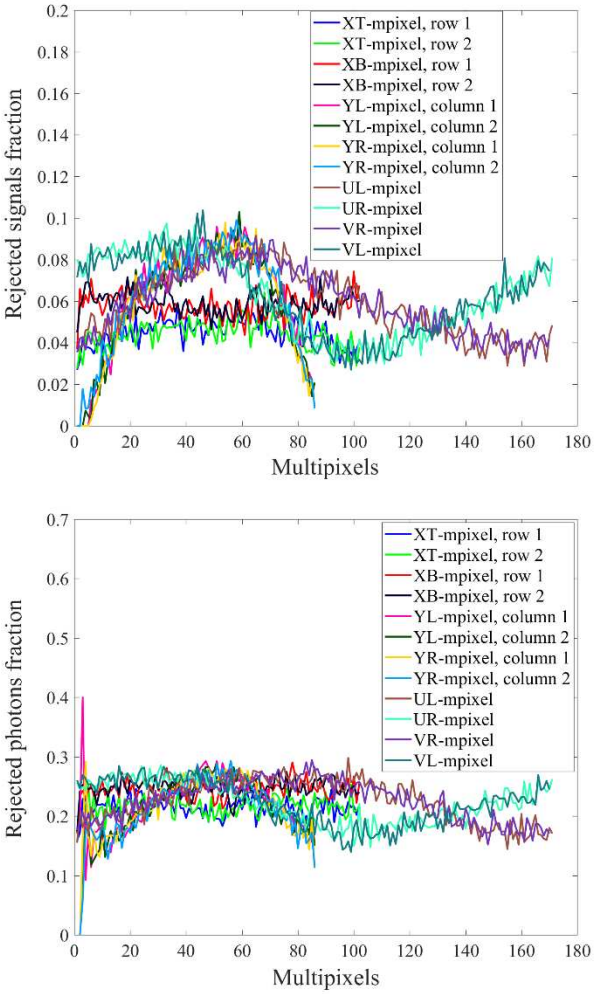

Figure 15. Top: fraction of the overlapped signals on each group of multipixels. Bottom: fraction of the rejected photons for each group of multipixels.

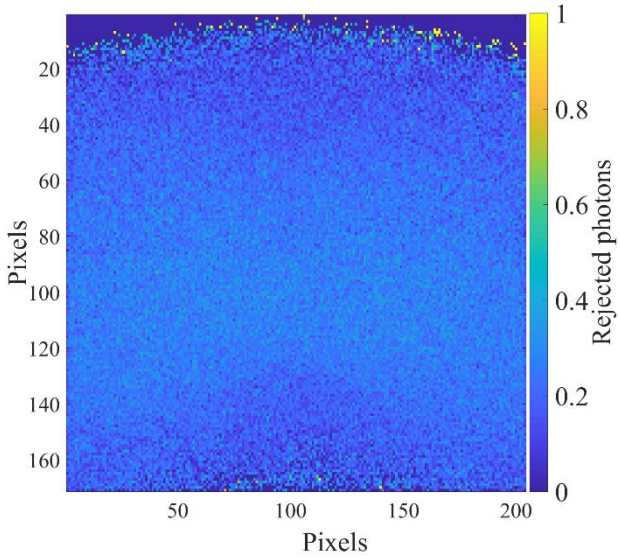

Figure 16. 2D map of the rejected photons for the considered multipixels. The mean value for the central most intensive part is about 25%.

The map of the rejected photons is shown in Figure 16. The average percentage of the overlapped signals was found to be at the level of 25% for the central most intensive part of the detecting surface (within rows from 40 till 140). It should be mentioned that the obtained numbers of the lost photons (up to about 25%) are quite promising. Comparing the recently obtained results presented in [10] and considering much smaller irradiated surface involved in the experiment described therein, it could be concluded that the proposed structure could fulfil high requirements implied by plasma radiation measurements. The fact worth reminding is that the conducted study was performed for the GEM detector rate capability limits. The further optimization of the pixel size and pixels interconnection could improve the obtained results even further.

5. Summary

Application of the GEM based detector in plasma physics requires its operation with high rate capability, close to its space charge limit (~10^5 Hz/mm^2). Within the present work, in case of the full power scenario, the expected radiation intensity is far above this limit. Therefore, an effort was taken to develop readout anode structure suitable for tokamak plasma imaging at the limit values for the considered detectors. In this study the goal was to achieve such a readout structure that would be capable to fulfil both conditions: (1) to collect (i.e. to determine energy and position) as many absorbed photons as possible up to the detector limits, and (2) to have reasonable number of the independent channels of electronics. To reduce this number to a reasonable one, in terms of costs and data processing, an interconnection between pixels was implemented in a special way to account for signals pile-up and to maximize the board effectiveness. Here, considering symmetry of the detector avalanche and the calculated spatial distribution of the plasma radiation, the presented scheme was studied as the first approach.

Summarizing the achievements of the present work, it is worth noting that for the considered readout structure the total amount of rejected counts due to overlapping of the detector signals was at the level of about 25% for the central, most irradiated, part of the detecting area. Based on the authors' experience the proposed anode structure should provide quite effective plasma radiation imaging. Further optimization of the anode board could be performed for the specific plasma scenarios and eventual experimental set-up. Additionally, some tuning of the size of the pixels and further optimization of the multipixels groups could also be performed.

Acknowledgments

This scientific work was partly supported by the Polish Ministry of Science and Higher Education within the framework of the scientific financial resources in the year 2020 allocated for the realization of the international co-financed project No 5118/H2020/EURATOM/2020/2.

This work has been carried out within the framework of the EUROfusion Consortium and has received funding from the Euratom research and training programme 2014-2018 and 2019-2020 under grant agreement No 633053. The views and opinions expressed herein do not necessarily reflect those of the European Commission.

References

[1] F. Crisanti et al., „The DTT device: Rationale for the choice of the parameters," Fusion Engineering and Design 122 (2017) 288-298.

[2] A. Kallenbach et al., „Tokamak operation with high-Z plasma facing components," Plasma Phys. Control. Fusion 47 (2005) B207.

[3] A.Loarte, R.Neu, „Power exhaust in tokamaks and scenario integration issues," Fusion Engineering and Design 122 (2017) 256–273.

[4] R. Albanese et al., „The DTT proposal. A tokamak facility to address exhaust challenges for DEMO: Introduction and executive summary," Fusion Engineering and Design 122 (2017) 274–284.

[5] F. Sauli, „The gas electron multiplier (GEM): Operating principles and applications," Nuclear Instruments and Methods A 805 (2016) 2-24.

[6] A. Karadzhinova et al., „Impact of GEM foil hole geometry on GEM detector gain," Journal of Instrumentation 10 (2015) P12014.

[7] O. Bouianov et al., „Foil geometry effects on GEM characteristics," Nuclear Instruments and Methods A 458 (2001) 698.

[8] M. Chernyshova et al., „Study of the optimal configuration for a Gas Electron Multiplier aimed at plasma impurity radiation monitoring," Fusion Engineering and Design 134 (2018) 1-5.

[9] M. Chernyshova et al., „Development of GEM detector for tokamak SXR tomography system: Preliminary laboratory tests," Fusion Engineering and Design 123 (2017) 877.

[10] M. Chernyshova et al., „2D GEM based imaging detector readout capabilities from perspective of intense soft x-ray plasma radiation," Review of Scientific Instruments 89 (2018) 10G106.

[11] A.F. Buzulutskov, „Radiation Detectors Based on Gas Electron Multipliers," Instruments and Experimental Techniques 50 (2007) 287–310.

[12] A. Bressan et al., „Two-dimensional readout of GEM detectors," Nuclear Instruments and Methods A 425 (1999) 254.

[13] M. Ziegler et al., „A triple GEM detector with two-dimensional readout," Nuclear Instruments and Methods A 471 (2001) 260–263.

[14] G.V. Yushmanov, P.N. Pereverzev, „ASTRA automated system for transport analysis in a tokamak," IPP Report 5/98, 2002.

[15] G.M. Staebler et al., „Gyro-landau fluid equations for trapped and passing particles," Physics of Plasmas 12 (2005) 102508.
[16] G.M. Staebler et al., „A theory-based transport model with comprehensive physics," Physics of Plasmas 14 (2007) 055909.
[17] G.M. Staebler et al., „The role of zonal flows in the saturation of multi-scale gyrokinetic turbulence," Physics of Plasmas 23 (2016) 062518.
[18] M. Romanelli et al., „JINTRAC: a system of codes for integrated simulation of tokamak scenarios," Plasma and Fusion Research 9 (2014) 3403023.
[19] S. Saarelma et al., „Integrated modelling of H-mode pedestal and confinement in JET-ILW.," Plasma Physics and Controlled Fusion 60 (2017) 014042.
[20] P. Snyder et al., „A first-principles predictive model of the pedestal height and width: development, testing and ITER optimization with the EPED model," Nuclear Fusion 51 (2011) 103016.
[21] I. Casiraghi et al., „First-principle based multi-channel integrated modelling in support to the design of the Divertor Tokamak Test Facility," Nuclear Fusion, to be submitted.
[22] S. Jablonski et al., „Simulation of pulse height analysis soft X-ray spectra expected from W7-X," Journal of Instrumentation 10 (2015) P10021.
[23] R.D. Gill et al., „Soft X-ray measurements of the impurity density in DITE," Nuclear Fusion 19 (1979) 1003.
[24] E. H. Silver et al., „Soft X-ray measurements from the PDX tokamak," Review of Scientific Instruments 53 (1982) 1198.
[25] S. Von Goeler et al., „Thermal X-ray spectra and impurities in the ST Tokamak," Nuclear Fusion 15 (1975) 301.
[26] D. Pasini et al., „JET X-ray pulse-height analysis system," Review of Scientific Instruments 59 (1988) 693.
[27] A. Weller et al., „Modelling of soft X-Ray emission from JET plasmas," JET Report, JET Joint Undertaking internal, Report JET-IR-(87)10 (1987).
[28] A. Burgess, „A general formula for the estimation of dielectronic recombination coefficients in low-density plasmas," Astrophysical Journal 141 (1965) 1588.
[29] R. Mewe, „Interpolation formulae for the electron impact excitation of ions in the H-, He-, Li-, and Ne-sequences," Astronomy and Astrophysics 20 (1972) 215.
[30] E. Gullikson, „X-Ray interactions with matter," [Online]. Available: https://henke.lbl.gov/optical_constants [access date: 01 11 2020].
[31] S. Agostinelli et al., „Geant4 - a simulation toolkit," Nuclear Instruments and Methods A 506 (2003) 250.
[32] K. Malinowski et al., „Simulation of energy spectrum of GEM detector from an x-ray quantum," Journal of Instrumentation 13 (2018) C01018.
[33] G. Knoll, „Radiation Detection and Measurement," John Wiley & Sons, New York U.S.A., 2000.
[34] M. Chernyshova et al., „Development of GEM detector for plasma diagnostics application: simulations addressing optimization of its performance," Journal of Instrumentation 12 (2017) C12034.
[35] A. Wojenski et al., „Multichannel measurement system for extended SXR plasma diagnostics based on novel radiation-hard electronics," Fusion Engineering and Design 123 (2017) 727-731.
[36] T. Czarski et al., „The cluster charge identification in the GEM detector for fusion plasma imaging by soft X-ray diagnostics," Review of Scientific Instruments 87 (2016) 11E336.
[37] A. Wojenski et al., „Multichannel reconfigurable measurement system for hot plasma diagnostics based on GEM-2D detector," Nuclear Instruments and Methods B 364 (2015) 49–53.